Dynamic changes on Wilkins Ice Shelf during the 2006-2009 retreat derived from satellite observations

Melanie Rankl[1], Johannes Jakob Fürst[1], Angelika Humbert[2/3], Matthias Holger Braun[1]

[1]Friedrich-Alexander Universität Erlangen-Nürnberg, Institute of Geography, 91058 Erlangen, Germany
5 [2]Alfred Wegener Institute, Helmholtz Centre for Polar and Marine Research, Glaciology Section, 27568 Bremerhaven, Germany
[3]University of Bremen, Department of Geosciences, 28359 Bremen, Germany

Correspondence to: Melanie Rankl (melanie.rankl@fau.de)

Abstract. Ice shelves serve as important buttresses for upstream areas. Several large ice shelves on the Antarctic Peninsula have disintegrated or retreated, which implied dynamic consequences for upstream ice. The present study aims to assess dynamic
10 changes on Wilkins Ice Shelf during multi-stage ice-front retreat in the last decade. A total area of 2135 ± 75 km² was lost in the period 2008-2009. The present study uses time-series of SAR satellite observations (1994/96, 2006-2010) in order to derive variations in multi-temporal surface flow from intensity offset tracking methods. Spatial patterns of horizontal strain rate and stress components were inferred during different ice-front retreat stages. These fields are used to explain the different break-up stages and to evaluate the ice-shelf stability. For this purpose, we apply criteria which were forwarded to explain and assess past ice-shelf
15 retreat.

1 Introduction

Antarctic ice shelves are sensitive indicators for global climate change (Vaughan and Doake, 1996). Ice-shelf collapse or break-up led to tributary-glacier acceleration and dynamic thinning (Berthier et al., 2012; Rignot, 2004; Scambos, 2004). The reason is that ice shelves restrain the outflow from tributary glaciers, thus they serve as natural buttresses (De Angelis and Skvarca, 2003;
20 Khazendar et al., 2015; Rott et al., 2002; Scambos et al., 2014). Outflow increase becomes sea-level relevant when it reaches a key upstream location, the grounding line (Rignot, 2004; Shuman et al., 2011). This line pins down the location where ice becomes afloat on its general way towards the ocean. On the Antarctic Peninsula (AP), 12 major ice shelves have either disintegrated or significantly retreated (Doake and Vaughan, 1991; Rott et al., 2002; Scambos et al., 2003, 2000). In addition, many of these ice shelves experienced important thinning over the past two decades (Fricker and Padman, 2012; Paolo et al., 2015; Wouters et al.,
25 2015; Zwally et al., 2005). Ice shelves along the western coast of the AP exhibit thinning rates that are often twice as high as those on the eastern side (e.g., Larsen Ice Shelf) (Paolo et al., 2015). 87 % of the tributary glaciers showed retreating tongues (Cook, 2005). Reasons for this regionally concentrated ice shelf recession or break-up are manifold. Explanations range from a warming atmosphere (O'Donnell et al., 2011; Steig et al., 2009; Vaughan et al., 2003), to a reduction in sea ice coverage on the western side of the AP (Stammerjohn et al., 2008), to rising ocean temperatures on the Bellingshausen Sea continental shelf (Martinson et al.,
30 2008; Meredith and King, 2005) and to warming deep waters in the Weddell Sea (Robertson et al., 2002).

As it is long known that ice shelves serve as natural buttresses (De Angelis and Skvarca, 2003; Khazendar et al., 2015; Rott et al., 2002; Scambos et al., 2014), there were regular attempts to assess their structural stability under ice-front recession. A first criterion was formulated after final collapse of Larsen A, within only one week, and during the subsequent gradual recession of Larsen B. Doake et al. (1998) inferred all horizontal strain-rate components. The sign of the smaller eigenvalue of the strain-rate tensor was
35 then used to determine a line, downstream of which the ice-flow regime is exclusively extensive (all eigenvalues positive). This 'compressive arch' was forwarded as a threshold contour for frontal recession, beyond which ice shelves are expected to ultimately

disintegrate. In the meantime, ice-flow models were successfully applied to get a more comprehensive description, including the stress distribution. Studying Larsen C ice shelf, Kulessa et al. (2014) proposed that ice-shelf stability should be assessed from the stress-flow angles. It is the angle between ice-flow direction and the first principal stress direction. When the two align, fracture opening rates were considered to maximize. If angles are small near the ice front, this would be considered a less stable state.

5   Also relying on the stress regime within the ice, Fürst et al. (2016) quantified the maximum buttressing potential of all ice shelves in Antarctica. Though not addressing the stability issue, they could show that ~13 % of all floating ice is dynamically not relevant. Once ice-front recession exceeds this passive shelf-ice area, dynamic consequences are expected. For ice shelves in the Bellingshausen Sea, only a small 5 %-fraction can still be removed without dynamic implications.

The aim of this study is to assess changes in the dynamic state of Wilkins Ice Shelf (WIS) under the multi-stage break-up during

10   the last decade. For this purpose, ice-velocity maps are inferred from radar satellite observations in 1994/96 and 2006-2010. From these maps, we infer strain rates and the principal stress distribution. These fields will then help to explain the collapse stages, which allows us to assess the stability criteria forwarded in the literature (Doake et al., 1998; Fürst et al., 2016; Kulessa et al., 2014).

2 Study area

15   WIS is located at the south-western part of the AP covering an area of 10,150 km² in April 2015. The ice shelf is confined by Alexander, Rothschild and Latady Island. Mass gain at WIS is dominated by surface accumulation (Vaughan et al., 1993). Further contribution of mass originates from the main in-flow from Lewis Snowfield south-west of the ice shelf. Contribution of mass from Gilbert Glacier and two inlets, called Schubert and Haydn inlets, is highly restraint by prominent ice rises (e.g. Dorsey Island). During the last decades, WIS has undergone significant dynamic changes: Surface lowering of in total -4.95 ± 0.21 m between

20   1978 and 2008 at the southern WIS (Fig. 1) was found to be the largest for all AP ice shelves (Fricker and Padman, 2012). In recent years (2000-2008), however, thinning rates were less negative or even slightly positive at the northern WIS (Paolo et al., 2015). Average thickness changes at WIS account for -0.62 ± 0.12 m a^{-1} for the period 1994-2012 derived from radar altimetry and were attributed to basal melting (Paolo et al., 2015). Basal melt rates of WIS were estimated by several authors: Holland et al. (2010) found 0.66 m a^{-1} averaged over the period 1979 to 2007, Padman et al. (2012) inferred rates of 1.3 ± 0.4 m a^{-1} during 1992-2008,

25   while Rignot et al. (2013) derived 2003-2008 average rates of 1.5 ± 1 m a^{-1}.

In addition, major ice-front retreat has been detected (Braun et al., 2009; Scambos et al., 2000). Based on the analysis of multi-temporal satellite imagery and historic maps, several break-up stages were quantified (Arigony-Neto et al., 2014). Several causes for break-up at WIS were proposed in the literature: fracture formation due to bending stresses in combination with surface melt or brine infiltration (Scambos et al., 2009), transoceanic infragravity waves which induce fractures at Antarctic ice shelves

30   (Bromirski et al., 2010) and break-up due to bending stresses caused by enhanced basal melt (Braun and Humbert, 2009; Humbert et al., 2010). Continuous ice-front retreat led to the formation of a remnant ice connection between Latady and Charcot Island at the western WIS (ice bridge in Fig. 1a), which collapsed in April 2009. Braun et al. (2009) also documented the development of fractures and rifts as well as the role of ice rises in the break-up processes on WIS. Between 28/29 February and 30/31 May 2008, an area of 585 km² broke-off narrowing the connection between these two confining islands (Braun et al., 2009). In June/July 2008,

35   1220 ± 75 km² of ice was lost at the eastern side of this ice bridge (Fig. 1a), meaning further weakening of it (Humbert and Braun, 2008). Braun and Humbert (2009) found highly variable ice thicknesses (~250-170 m) along the ice bridge implying important buoyancy differences. The break-up events in May and June/July 2008 have demonstrated that such events can occur in austral winter (Braun et al., 2009). This contradicts previous assumptions that ice-shelf break-up depends on summer surface melt ponds

(Doake and Vaughan, 1991; MacAyeal et al., 2003; Scambos et al., 2009). In early April 2009, the final ice-bridge collapse corresponded to an area loss of 330 km². More than 100 tabular icebergs calved off. Many of these icebergs capsized, releasing an energy of >125 x 10^6 J (Humbert et al., 2010). After the collapse of the ice bridge, small-size calving events occurred, which primarily took place along the south-west ice front between Latady Island and Lewis Snowfield.

3 Material and Methods

3.1 SAR intensity offset tracking

Surface velocities of the ice shelf and its tributary glaciers were derived from SAR (Synthetic Aperture Radar) intensity offset tracking (Strozzi et al., 2002) using repeat ALOS PALSAR (46 day time interval) and ERS-1/-2 (35 day time interval) SAR Single Look Complex (SLC) image pairs (Table S1). This technique cross-correlates the backscatter intensity pattern of a pair of SAR images of different acquisitions dates. For this purpose, small image patches are shifted over the entire image (Table 1) and for each patch, the maximum of the 2-D cross-correlation function yields the image offsets in range and azimuth directions. If coherence between both image patches is retained, the speckle pattern is additionally correlated. Offsets of minor confidence were rejected based on a signal-to-noise-ratio (SNR ≤ 4). The processing was performed using Gamma Remote Sensing software. Geocoding of the final range and azimuth offsets from SAR to map geometry was based on the WGS84 ellipsoid.

The method relies on surface patterns which are identifiable in both images. However, co-registration and intensity offset tracking performed on single scenes of structure-less ice shelves was hardly successful. Therefore, single scenes along the respective relative orbits were concatenated (Fig. S1). Additionally, we used a binary mask of non-moving (e.g., ice rises, bedrock) and moving areas (ice shelf, tributary glaciers, sea) to perform co-registration on stable areas only (Fig. S1). In a post-processing step, the surface flow was filtered using a 5 x 5 pixel median filter and a threshold discarding flow vectors deviating from a reference direction applied.

For each year, several displacement fields of different relative orbits were mosaicked. Results in 1994/96 were taken from InSAR (Interferometric Synthetic Aperture Radar) derived surface flow presented in Braun et al. (2009) and from ERS-1/-2 intensity tracking. For each absolute flow field between 2006 and 2010, a mosaic of three to four relative ALOS PALSAR orbits represent the surface flow for the respective time period, mostly in austral summer (August/September to October/November in 2007-2010, Table S1). Ice flow in 2006 covers the period mid-May to mid-June. Due to the time difference between image acquisitions, the mosaicked surface flow shows slight deviations in the flow magnitude at the boundaries of each relative orbit. Hence, flow differences were calculated solely for the south-western orbit in order to show results independent from overlapping velocity results.

The estimation of errors in the derived velocity fields was done as described in McNabb et al. (2012) and in Seehaus et al. (2015). For each velocity field a value based on the accuracy of the co-registration was calculated and a second value described uncertainties involved in the intensity tracking algorithm (Table S2).

3.2 Stress tensor and strain rates

In order to infer the components of the stress tensor associated with a flow field, a constitutive equation is required. In glaciology, ice is typically described as being a non-Newtonian fluid with a viscosity η depending on temperature and effective strain rate. In its most general form, the constitutive equation for the deviatoric stress τ_{ij} can be written as follows:

$$\tau_{ij} = 2\eta \cdot \dot{\varepsilon}_{ij} \tag{1}$$

Here, $\dot{\varepsilon}$ is the strain-rate tensor, which holds information on spatial derivatives of the horizontal velocity field:

$$\dot{\varepsilon}_{ij} = \frac{1}{2}\left(\frac{\partial u_i}{\partial x_j} + \frac{\partial u_j}{\partial x_i}\right) \tag{2}$$

The strain-rate tensor describes how much the ice is deformed at a certain location and its horizontal components can be inferred from surface velocities. For the purpose of understanding the changes in the stress regime due to the break-up events, it is of particular importance to look at strain rates and not velocity fields. Velocity fields are derived by measuring displacements of features assuming that the features themselves do not change. In case of opening of a rift, the feature is often a rift face or a crack front, and both change over time. Thus, the interpretation of the displacement field as a flow velocity can only be done in case there is no rift opening. Otherwise, the displacement due to opening of a rift and the creep of ice are superimposed in the velocity field. Strain rates, however, overcome this flaw, as they are spatial derivatives.

The ice viscosity then determines how strain rates translate into deviatoric stresses τ_{ij}. Stress deviators are linked to the full Cauchy stress $\boldsymbol{\sigma}$ by adding the isometric pressure.

$$\tau_{ij} = \sigma_{ij} - \frac{1}{3}\delta_{ij}\sum_k \sigma_{kk} \quad \text{(Pattyn, 2003)} \tag{3}$$

At the ice-shelf surface (denoted as superscript s in the following), where satellite data is acquired, the relation between deviatoric and full stresses simplifies to:

$$\sigma_{xx}^s = 2\tau_{xx}^s + \tau_{yy}^s \tag{4}$$

$$\sigma_{yy}^s = \tau_{xx}^s + 2\tau_{yy}^s \tag{5}$$

This assumes that horizontal bridging effects are negligible near the ice surface. At the ice surface, the horizontal Cauchy stress components are a sum of the horizontal deviatoric stress components, which in turn can be inferred from the strain fields. Therefore our discussion is limited to the surface conditions of the ice shelf. In the following, however, we will often omit to specify this limitation and simply speak of strain and stress conditions.

In addition, the viscous response of an ice body is not necessarily linear and depends itself on the strain regime:

$$\eta = \frac{1}{2}mA^{-1/n} \cdot \dot{\varepsilon}_e^{(1-n)/n} \tag{6}$$

Here, $\dot{\varepsilon}_e^2 = \frac{1}{2}[(\text{tr}(\dot{\varepsilon}))^2 - (\text{tr}(\dot{\varepsilon}^2))]$ is the second invariant of the strain-rate tensor. We assume isotropic material properties and a flow exponent of $n = 3$. A is the rate factor, which determines the readiness of the viscous material to deform under a given stress (Van der Veen, 2013). For WIS, we assume a constant rate factor A of 1.7×10^{-24} Pa^{-3} s^{-1} (Cuffey and Paterson, 2010) corresponding to temperate ice of about -2° C as observed in this area (Braun et al., 2009). The rate factor is generally a function of ice temperature and microscopic water content and consequently varies on ice-shelf scales. The enhancement factor m is assumed constant and set to 1. In general, m is, however, a function of grain size, impurities, damage degree and other variables (Cuffey and Paterson, 2010, p. 71). These additional factors are difficult to account for and are therefore not reflected in the subsequently presented stress fields. However, the zero stress line remains unaffected by this scaling issue.

Strain and stress components are real and, by construction, the strain rate and stress tensors are symmetric. Therefore, all eigenvalues are also real. Moreover, we order the two eigenvalues for each tensor by size. In general, the larger eigenvalue of these tensors is referred to as the first principal component (Doake et al., 1998; Kulessa et al., 2014). First and second principal components span the range of minimal and maximal extensive or compressive strain rates or stress occurring at the ice surface. The first principal strain rate gives maximal extension rates and is therefore of interest to define a crevasse initiation or material failure criteria (Benn et al., 2007; see Vaughan, 1993). Observed threshold-strain rates for fracture initiation span a wide range from 0.01 a^{-1} (2.7E-5 day^{-1}) on Greenland (Meier, 1958) to 0.004 a^{-1} (1.0E-5 day^{-1}) on White Glacier, Canada (Hambrey and Müller, 1978). To describe damage initiation within an ice body, Krug et al. (2014) used a threshold criterion for the first principal stress component. In terms of stresses, inferred thresholds range from 90 to 320 kPa (Vaughan, 1993). The Hayhurst rupture

criterion defines a stress threshold of 330 kPa for fracture initiation (Pralong et al., 2006). Second principal surface stress, however, was recognized to be important in terms of ice-shelf stability (Doake et al., 1998) or, more general, to assess and quantify the dynamic susceptibility of ice shelves (Fürst et al., 2016).

4 Ice dynamic changes

4.1 Results

Break-up at WIS was analysed using multi-temporal surface flow in 1994/96 and between 2006 and 2010 (Fig. 2). Figure 3 shows the period between 2006 and 2009 in more detail, when the ice bridge gradually collapsed.

The general picture of surface flow shows prominent inflow from Gilbert Glacier, Haydn and Schubert inlets, and directly from Lewis Snowfield over all years 1994/96 and 2006-2010 (Fig. 2), where flow rates can exceed 1.5 m day^{-1}. The inflow is, however, restrained and deviated for instance by Dorsey Island or by the ice rises in front of Haydn and Schubert inlets.

The entire ice shelf showed very small velocities in March 1994/96. Slightly higher surface motion was encountered in the south-west, originating from Lewis Snowfield as well as near the ice front at Charcot Island after the 1993 break-up event (remnant icebergs are still visible in the backscatter SAR image in Fig. 2a). Between February and June 1998, a large double fracture formed almost parallel to the western ice front of the ice bridge between Latady and Charcot Island (green line in Fig. 3a). In July 2007, surface flow on the ice bridge increased due to the formation of the second longitudinal fracture-pair (purple line in Fig. 3e). This acceleration was followed by major ice loss on the western and south-eastern ice bridge between February and July 2008 (Braun and Humbert, 2009; Humbert et al., 2010). A total area of 1805 ± 75 km² was lost. The consecutive acceleration was most expressed on the ice bridge (up to ~0.8 m day^{-1} at the narrowest part), but did certainly reach as far upstream as to the Petrie Ice Rises (Fig. 2g). Upstream of this region, acceleration is somewhat lower. The north-western part of the ice bridge remained rather stagnant, still experiencing and transmitting the buttressing from Charcot Island (Fig. 3i). The narrow remainder of the ice bridge finally collapsed in April 2009 and an area of 330 km² broke off (Humbert et al., 2010). This final event caused almost no additional upstream acceleration (Fig. 2h). This suggests that the lost ice-shelf portion did not transmit or provide an important restraint to the central ice-shelf unit. In 2010, results from feature tracking were unavailable for some parts of the WIS and the coverage was incomplete (Fig. 2f). Yet, from the covered areas of the ice shelf, we are confident that ice flow did not change significantly between 2009 and 2010 (Fig. 2e, f). In addition, the ice-front position remained stable during this period (Fig. 2f).

From the strain-rate tensor, we inferred the component pointing in flow direction. This in-flow strain rate gives an indication on whether the flow regime is extensive or compressive along streamlines. Yet, the quality of the in-flow strain rate is highly dependent on the reliability of the inferred flow directions. Very low flow speeds, as found on the main ice shelf in 2006 and 2007, are more susceptible to errors (Fig. 3a, e). Thus, for the interpretation of in-flow strain-rates, we will limit the discussion to areas showing considerable motion.

The in-flow strain-rate component is negative in all years 2006-2009, where the ice flow is blocked by an obstacle, e.g., upstream of the Petrie Ice Rises (Fig. 3b, f, j, n; compressive strain rates correspond to negative values). Compressive strain rates also prevail close to Latady Island, where a slight inflow is visible (Fig. 3b, f, j, n). Extension and thus positive strain rates dominate in 2006 and 2007 along the ice bridge (Fig. 3b, f; red values indicate extensive strain). In 2008, most parts of the ice shelf show extensive flow, merely buttressed by the Petrie Ice Rises and Latady Island (Fig. 3j). In-flow strain rates of opposite sign on each side of the narrowest part of the ice bridge in 2008 explain the formation of an initial crack and why the ice bridge failed there. The prevailing atmospheric circulation pushed the brittle ice mélange westward, which was forwarded as a reason for why the bridge yielded in this direction (Humbert et al., 2010).

The first principal strain rate gives the maximum stress value (Fig. 3c, g, k, o). It is positive all over the ice shelf in all years, which means that the ice experiences extensive stress in a certain direction. Local maxima, i.e. maximum extension, occur on the lee side of ice rises and where fractures formed on the ice bridge in 2007 (Fig. 3g) and alongside Vere Ice Rise in 2008 (Fig. 3k).

The second principal strain-rate component is negative in all years (Fig. 3, lower panels). This implies that the flow regime of WIS
5   has a compressive component almost everywhere. As ice flow accelerates from 2006 to 2008, the second principal strain rate becomes less negative (Fig. 3d, h, l). After the final collapse of the ice bridge, this strain-rate component drops down again to pre-collapse values near the ice front and close to Latady Island (Fig. 3p).

Based on the calculation of surface flow in 2006-2009 and the basic assumption of a constant rate factor, principal stress fields were derived in order to assess the fundamental changes in the stress regime during the ice bridge break-up. The first principal
10   stress gives the highest extensive stress acting within the material. In all years 2006-2009, first principal stresses are generally positive (Fig. 4a, d, g, j). Local maxima in these fields coincide with fractures. It is not surprising that these maxima are often located at the tip of these fractures, where extensive forces are focused. In 2008 and 2009, however, a wave-like pattern becomes visible on the main part of the ice shelf (Fig. 4g, j). These artefacts cannot be explained by processes occurring in the ice, but might be inherent to the satellite data (e.g., ionospheric noise (Gray et al., 2000; Meyer et al., 2006) or might result from the tracking
15   algorithm.

The second principal stress holds information on the smallest extensive or largest compressive stress acting within the ice. For positive values, the ice-shelf surface experiences an exclusively extensive stress regime. In 2006 and 2007, a compressive second principal stress regime prevails on WIS (Fig. 4b, e). During the formation of the second double fracture on the ice bridge in 2007 (purple line in Fig. 4d), this region turns fully extensive in terms of stresses as well as first principal strain rates (Figs. 3g & 4e).
20   Without any compressive components, the ice bridge was destined to split in two and the western part collapsed soon thereafter. In 2008, ice flow increased and with it the second principle stress. In large areas previously showing negative values, the stress regime turned entirely extensive in 2008 (Fig. 4h). The only exceptions are the vicinity of ice rises and near Latady Island. One year later, the stress state has reverted back to the pre-acceleration state with a largely compressive second principal component (Fig. 4k).
25   Assessing ice-shelf stability on Larsen C, Kulessa et al. (2014) introduced a new variable. They computed the angle between the ice-flow direction and the first principal stress direction. They argue that when flow direction and first principal stress direction align, fracture formation is facilitated. This stress-flow angle is consequently used as a criterion for ice-shelf stability, which we follow here for comparison. Low stress-flow angles indicate areas, which are more likely to suffer from break-up, whereas larger stress-flow angles, approaching 90°, indicate stable conditions (Jansen et al., 2015). Stress-flow angles on WIS are small, where
30   fractures formed, e.g., on the ice bridge in 2007 or upstream the ice bridge, parallel to the northern ice front in 2008 (Fig. 4f, i). Stress-flow angles on the ice bridge, however, show higher values in 2008 (Fig. 4i).

4.2 Assessing the retreat stages

In this section, we want to investigate, which fields are more or less informative, when it comes to identifying weaknesses and predicting the next break-up stage.
35   In 2006, no field shows any indication that another fracture pair would open. Near the existing double fracture, which formed in 1998 (Fig. 3a) local maxima are discernible for in-flow strain rates (Fig. 3b) and the first and second principal stresses (Fig. 4a, b). The latter stress even turns positive. Neither the second principal strain rate nor the stress-flow angle shows a well imprinted trace of the already present fracture.

Turning to 2007, most fields reflect the opening of the new fracture pair on the ice bridge (Figs. 3 & 4). Only exception is the second principal strain rate (Fig. 3h). From the ice velocities, it is obvious that the western part of the ice bridge started to accelerate and will soon disintegrate. None of the derived fields allows such a clear distinction of the bridge sides. An explanation is that all other variables are derived from spatial derivatives of the flow field. Despite this distinction, the strain field in flow direction turned

5   compressive along the old fracture pair on the eastern part of the bridge (Fig. 3f). In the principal stress components we can discern a local stress maxima (pure extension) on the southwestern trunk of the ice bridge (Fig. 4d, e), which could explain fracturation there.

Stress-flow angles show very small values on the north-western end of the bridge (Fig. 4f). Following the interpretation from Kulessa et al. (2014), fracture opening would be facilitated. In this area, first principal stress components are not particularly

10   elevated (Fig. 4d). The stress-flow angle criteria is, however, the only measure that points out instable conditions all along the north-eastern ice front, which actually retreated afterwards. Low values along the south-western ice front might be an artefact from not well constrained flow directions (Fig. 4f).

By 2008, ice flow fundamentally changed both in terms of direction and magnitude. All measures reflect this important change. The in-flow strain rates show different flow regimes on each side of the narrowest part of the ice bridge: upstream extension vs.

15   downstream compression (Fig. 3j). This explains the later failure position. No other field can make an as clear distinction here. The second principal strain rate gradually increased since 2006 but still remains mostly negative (Fig. 3l). Even if zero is not passed, the stability interpretation from Doake et al. (1998) would suggest reduced retreat susceptibility as compared to the previous stages. However, the ice bridge was lost afterwards. The stress-flow angles suggest a different interpretation of this state. High values dominate on the ice bridge, while all the rest of the north-eastern ice front shows small angles (Fig. 4i). The interpretation

20   of these angles would suggest that the ice bridge has a stabilizing effect on the upper more susceptible areas. This deduced stabilization could however not prevent the consecutive collapse. In this case, the interpretation of stress-flow angles is therefore delicate. Both for the Doake criterion and the stress-flow angle, the ice-shelf might already have adopted a flow regime consistent with the post-collapse ice front. An interpretation of the field downstream of the latter ice front position might be futile. For both principal stress components (Fig. 4g, h), as well as for the in-flow strain rates (Fig. 3j), values are highly elevated along the

25   fractures, which later became the new north-eastern ice-front position.

The state in 2009 points towards stable conditions on WIS reflected in all measures. To date, no further ice-front retreat occurred at the northern ice front.

4.3 Ice-shelf stability

From the above assessment, some of the presented measures emerge to be more or less applicable for assessing ice-shelf stability.

30   The most intuitive measure for interpreting the retreat stages might be the in-flow strain rates (Fig. 3) and the principal stress components (Fig. 4). Sign changes and local maxima in these strain-rate fields could be exploited in this interpretation. The fist principal strain-rate component can be used to describe a crevasse opening threshold on ice shelves. Local strain-rate maxima on the ice bridge in 2007 (Fig. 3g) and perpendicular to the ice bridge in 2008 (Fig. 3k) reach maxima between ~5E-5 and 1.3E-4 day^{-1}. The narrowest part of the ice bridge holds maximum first principal strain rates of ~1.2E-4 day^{-1} in 2008. Threshold strain rates

35   determined for crevasse opening on other glaciers (Hambrey and Müller, 1978; Meier, 1958) show comparable or even smaller values. Therefore, the latter fracturation and ice-shelf break-up can be explained.

For the interpretation of the second principal strain-rate component (Fig. 3, lowest panels), we want to follow Doake et al. (1998). They forwarded that when the ice front retreats/recedes beyond a certain isoline in this strain-rate component, the ice-shelf integrity is no longer granted and a destabilization is expected. The stress value associated to this isoline is suggested to be close to zero.

Second principal strain rates are rather insensitive during the retreat stages of WIS. Values are generally negative and therefore suggest general recession.

The first principal stress component points out regions, where fractures are likely to open or propagate (Krug et al., 2014; Vaughan, 1993). On WIS the threshold between 90 and 320 kPa mentioned above (Vaughan, 1993) holds for the break-up events in 2007 and 2008 (Fig. 4d, g). In 2007, the first principal stress regime on the ice bridge exceeded ~200 kPa as well as in 2008, when fractures parallel to the ice front formed (Fig. 4d, g). Values were slightly lower at the narrowest part of the ice bridge, where the ice bridge collapse initiated (Fig. 4g). Yet, the magnitude of this field scales directly with the rate factor, hence, any threshold criteria inferred from observations has to be considered with caution.

The second principal stress component shows some advantage in this respect (Fig. 4b, e, h, k). For all retreat stages, we confirm that this stress field shows a change in sign to positive values in critical regions. Such sign changes are unaffected by the rate factor choice. Thus, we think that positive second principal stresses add substantially to a pure strain-rate interpretation.

The stress-flow angle on WIS is rather ambiguous (Fig. 4 lowest panels). Though some retreat stages can be explained, this is certainly not the case for others. In defence of this measure, we have to add that the derivation of stress-flow angles shown in Kulessa et al. (2014) is based on modelled ice-shelf velocities, flow lines and stresses using a continuum-mechanical ice-flow model. In the present study, however, the angle is calculated from observations, which results in high spatial variability of the underlying principal strain-rate directions.

5 Conclusions

Our study revealed the potential of modern satellite missions to derive a comprehensive overview of dynamic changes on WIS before and during ice-shelf break-up. For this, multi-temporal velocity maps were derived for 1994/96 and 2006-2010. A considerable ice-flow speed up occurred after ice-front retreat in 2008. The estimation of principal strain-rate and stress components helped to identify ice-shelf areas prone to crevasse opening and fracture propagation during the individual stages of the ice bridge collapse between 2006 and 2009. These findings extend previous observations based on a qualitative analysis of satellite data. Directly inferable from surface velocities, the first principal strain rate as well as the strain rate in flow direction proofed valuable for interpreting the retreat stages. In terms of fracture initiation, the first principal surface stress could be exploited to infer where crevasses might open. However, this variable scales with the not well known ice viscosity. Independent of this scaling issue, positive values in the second principal surface stress highlight the regions susceptible to break-up. Other measures like second strain-rate regimes and the stress-flow angle proofed less appropriate to assess the subsequent retreat history and thus the ice-shelf stability.

The future stability of WIS is considered rather weak. Based on the analysis of several SAR images acquired in recent years (2011-2015) the formation of fractures at the south-western ice front was detected. In front of Lewis Snowfield, on the lee side of small ice rises, fractures have developed since 2011 (Fig. 1b) and have grown perpendicular to the south-western ice front since then. In August 2014, one of these fractures grew further towards the centre of the ice shelf, forming a kink parallel to the south-western ice front. Another fracture was detected on a Sentinel 1a imagery from April 2015, north of the ones described before (Fig. 1b). This fracture emerged perpendicular to the ice front towards the ice shelf centre. Further growth of the fractures towards the ice shelf centre and a connection of them, might lead to future loss of a large portion of the ice shelf and presumably a disconnection from Latady Island.

Author contributions

M.R. drafted the design of the study, collected the SAR data and calculated the velocity maps. J.F. calculated strain-rate and stress components as well as stress-flow angles. M.R. and J.F. analysed the results and wrote the manuscript jointly. The figures have been designed by M.R. The manuscript has been revised by M.B. and A.H. This work is embedded in a DFG project initiated by

5   M.B. and A.H.

Acknowledgements

Satellite data was kindly provided by DLR AO mabra_XTI_GLAC0264 and ESA AO 4032. The authors thank the Deutsche Forschungsgemeinschaft (DFG) for support in the framework of the priority program "Antarctic Research with comparative investigations in Arctic ice areas" under grant BR2105/8-1. M.B. received funding by the European Commission under the 7th

10   Framework Program through the action – IMCONet (FP7 IRSES, action No.319718), J.F. was supported by DFG grant FU1032/1-1. This work was embedded as co-funding activity within the HGF Alliance "Remote Sensing & Earth System Dynamics".

References

Arigony-Neto, J., Skvarca, P., Marinsek, S., Braun, M., Humbert, A., Júnior, C. W. M. and Jaña, R.: Monitoring Glacier Changes on the Antarctic Peninsula, in Global Land Ice Measurements from Space, pp. 717–741, Springer., 2014.

15   Benn, D. I., Warren, C. R. and Mottram, R. H.: Calving processes and the dynamics of calving glaciers, Earth-Sci. Rev., 82(3), 143–179, 2007.

Berthier, E., Scambos, T. A. and Shuman, C. A.: Mass loss of Larsen B tributary glaciers (Antarctic Peninsula) unabated since 2002, Geophys. Res. Lett., 39(13), L13501, doi:10.1029/2012GL051755, 2012.

Braun, M. and Humbert, A.: Recent Retreat of Wilkins Ice Shelf Reveals New Insights in Ice Shelf Breakup Mechanisms, IEEE

20   Geosci. Remote Sens. Lett., 6(2), 263–267, doi:10.1109/LGRS.2008.2011925, 2009.

Braun, M., Humbert, A. and Moll, A.: Changes of Wilkins Ice Shelf over the past 15 years and inferences on its stability, The Cryosphere, 3(1), 41–56, doi:10.5194/tc-3-41-2009, 2009.

Bromirski, P. D., Sergienko, O. V. and MacAyeal, D. R.: Transoceanic infragravity waves impacting Antarctic ice shelves: IG-WAVES IMPACTING ANTARCTIC ICE SHELVES, Geophys. Res. Lett., 37(2), doi:10.1029/2009GL041488, 2010.

25   Cook, A. J.: Retreating Glacier Fronts on the Antarctic Peninsula over the Past Half-Century, Science, 308(5721), 541–544, doi:10.1126/science.1104235, 2005.

Cuffey, K. M. and Paterson, W. S. B.: The physics of glaciers, Academic Press., 2010.

De Angelis, H. and Skvarca, P.: Glacier surge after ice shelf collapse, Science, 299(5612), 1560–1562, 2003.

Doake, C. S. M. and Vaughan, D. G.: Rapid disintegration of the Wordie Ice Shelf in response to atmospheric warming, Nature,

30   350(6316), 328–330, doi:10.1038/350328a0, 1991.

Doake, C. S. M., Corr, H. F. J., Rott, H., Skvarca, P. and Young, N. W.: Breakup and conditions for stability of the northern Larsen Ice Shelf, Antarctica, Nature, 391(6669), 778–780, 1998.

Fricker, H. A. and Padman, L.: Thirty years of elevation change on Antarctic Peninsula ice shelves from multimission satellite radar altimetry, J. Geophys. Res., 117(C2), doi:10.1029/2011JC007126, 2012.

35   Fürst, J. J., Durand, G., Gillet-Chaulet, F., Tavard, L., Rankl, M., Braun, M. and Gagliardini, O.: The safety band of Antarctic ice shelves, Nat. Clim Change, 6(5), 479–482, 2016.

Gray, A. L., Mattar, K. E. and Sofko, G.: Influence of ionospheric electron density fluctuations on satellite radar interferometry, Geophys. Res. Lett., 27(10), 1451–1454, doi:10.1029/2000GL000016, 2000.

Hambrey, M. J. and Müller, F.: Structures and ice deformation in the white glacier, Axel Heiberg Island, Northwest Territories, Canada, J. Glaciol., 20(82), 41–66, 1978.

5 Holland, P. R., Jenkins, A. and Holland, D. M.: Ice and ocean processes in the Bellingshausen Sea, Antarctica, J. Geophys. Res., 115(C5), doi:10.1029/2008JC005219, 2010.

Humbert, A. and Braun, M.: The Wilkins Ice Shelf, Antarctica: break-up along failure zones, J. Glaciol., 54(188), 943–944, doi:10.3189/002214308787780012, 2008.

Humbert, A., Gross, D., Müller, R., Braun, M., Van De Wal, R. S. W., Van Den Broeke, M. R., Vaughan, D. G. and Van De Berg,
10 W. J.: Deformation and failure of the ice bridge on the Wilkins Ice Shelf, Antarctica, Ann. Glaciol., 51(55), 49–55, 2010.

Jansen, D., Luckman, A. J., Cook, A., Bevan, S., Kulessa, B., Hubbard, B. and Holland, P. R.: Brief Communication: Newly developing rift in Larsen C Ice Shelf presents significant risk to stability, The Cryosphere, 9(3), 1223–1227, doi:10.5194/tc-9-1223-2015, 2015.

Khazendar, A., Borstad, C. P., Scheuchl, B., Rignot, E. and Seroussi, H.: The evolving instability of the remnant Larsen B Ice
15 Shelf and its tributary glaciers, Earth Planet. Sci. Lett., 419, 199–210, doi:10.1016/j.epsl.2015.03.014, 2015.

Krug, J., Weiss, J., Gagliardini, O. and Durand, G.: Combining damage and fracture mechanics to model calving, The Cryosphere, 8(6), 2101–2117, 2014.

Kulessa, B., Jansen, D., Luckman, A. J., King, E. C. and Sammonds, P. R.: Marine ice regulates the future stability of a large Antarctic ice shelf, Nat. Commun., 5, 2014.

20 MacAyeal, D. R., Scambos, T. A., Hulbe, C. L. and Fahnestock, M. A.: Catastrophic ice-shelf break-up by an ice-shelf-fragment-capsize mechanism, J. Glaciol., 49(164), 22–36, 2003.

Martinson, D. G., Stammerjohn, S. E., Iannuzzi, R. A., Smith, R. C. and Vernet, M.: Western Antarctic Peninsula physical oceanography and spatio–temporal variability, Deep Sea Res. Part II Top. Stud. Oceanogr., 55(18), 1964–1987, 2008.

Mcnabb, R. W., Hock, R., O'Neel, S., Rasmussen, L. A., Ahn, Y., Braun, M., Conway, H., Herreid, S., Joughin, I., Pfeffer, W. T.,
25 Smith, B. E. and Truffer, M.: Using surface velocities to calculate ice thickness and bed topography: a case study at Columbia Glacier, Alaska, USA, J. Glaciol., 58(212), 1151–1164, doi:10.3189/2012JoG11J249, 2012.

Meier, M. F.: The mechanics of crevasse formation, Gen. Assem. Tor. 1957-Snow Ice, 46, 500–508, 1958.

Meredith, M. P. and King, J. C.: Rapid climate change in the ocean west of the Antarctic Peninsula during the second half of the 20th century, Geophys. Res. Lett., 32(19), 2005.

30 Meyer, F., Bamler, R., Jakowski, N. and Fritz, T.: The Potential of Low-Frequency SAR Systems for Mapping Ionospheric TEC Distributions, IEEE Geosci. Remote Sens. Lett., 3(4), 560–564, doi:10.1109/LGRS.2006.882148, 2006.

O'Donnell, R., Lewis, N., McIntyre, S. and Condon, J.: Improved methods for PCA-based reconstructions: Case study using the Steig et al.(2009) Antarctic temperature reconstruction, J. Clim., 24(8), 2099–2115, 2011.

Padman, L., Costa, D. P., Dinniman, M. S., Fricker, H. A., Goebel, M. E., Huckstadt, L. A., Humbert, A., Joughin, I., Lenaerts, J.
35 T. M., Ligtenberg, S. R. M., Scambos, T. and van den Broeke, M. R.: Oceanic controls on the mass balance of Wilkins Ice Shelf, Antarctica, J. Geophys. Res., 117(C1), doi:10.1029/2011JC007301, 2012.

Paolo, F. S., Fricker, H. A. and Padman, L.: Volume loss from Antarctic ice shelves is accelerating, Science, 348(6232), 327–331, doi:10.1126/science.aaa0940, 2015.

Pattyn, F.: A new three-dimensional higher-order thermomechanical ice sheet model: Basic sensitivity, ice stream development,
40 and ice flow across subglacial lakes, J. Geophys. Res. Solid Earth, 108(B8), 2003.

Pralong, A., Hutter, K. and Funk, M.: Anisotropic damage mechanics for viscoelastic ice, Contin. Mech. Thermodyn., 17(5), 387–408, doi:10.1007/s00161-005-0002-5, 2006.

Rignot, E.: Accelerated ice discharge from the Antarctic Peninsula following the collapse of Larsen B ice shelf, Geophys. Res. Lett., 31(18), doi:10.1029/2004GL020697, 2004.

5   Rignot, E., Jacobs, S., Mouginot, J. and Scheuchl, B.: Ice-Shelf Melting Around Antarctica, Science, 341(6143), 266–270, doi:10.1126/science.1235798, 2013.

Robertson, R., Visbeck, M., Gordon, A. L. and Fahrbach, E.: Long-term temperature trends in the deep waters of the Weddell Sea, Deep Sea Res. Part II Top. Stud. Oceanogr., 49(21), 4791–4806, 2002.

Rott, H., Rack, W., Skvarca, P. and De Angelis, H.: Northern Larsen ice shelf, Antarctica: further retreat after collapse, Ann.
10   Glaciol., 34(1), 277–282, 2002.

Scambos, T., Hulbe, C. and Fahnestock, M.: Climate-Induced Ice Shelf Disintegration in the Antarctic Peninsula, in Antarctic Peninsula Climate Variability: Historical and Paleoenvironmental Perspectives, edited by E. Domack, A. Levente, A. Burnet, R. Bindschadler, P. Convey, and tthew Kirby, pp. 79–92, American Geophysical Union. [online] Available from: http://onlinelibrary.wiley.com/doi/10.1029/AR079p0079/summary (Accessed 26 September 2014), 2003.

15   Scambos, T., Fricker, H. A., Liu, C.-C., Bohlander, J., Fastook, J., Sargent, A., Massom, R. and Wu, A.-M.: Ice shelf disintegration by plate bending and hydro-fracture: Satellite observations and model results of the 2008 Wilkins ice shelf break-ups, Earth Planet. Sci. Lett., 280(1–4), 51–60, doi:10.1016/j.epsl.2008.12.027, 2009.

Scambos, T. A.: Glacier acceleration and thinning after ice shelf collapse in the Larsen B embayment, Antarctica, Geophys. Res. Lett., 31(18), doi:10.1029/2004GL020670, 2004.

20   Scambos, T. A., Hulbe, C., Fahnestock, M. and Bohlander, J.: The link between climate warming and break-up of ice shelves in the Antarctic Peninsula, J. Glaciol., 46(154), 516–530, 2000.

Scambos, T. A., Berthier, E., Haran, T., Shuman, C. A., Cook, A. J., Ligtenberg, S. R. M. and Bohlander, J.: Detailed ice loss pattern in the northern Antarctic Peninsula: widespread decline driven by ice front retreats, The Cryosphere, 8(6), 2135–2145, doi:10.5194/tc-8-2135-2014, 2014.

25   Seehaus, T., Marinsek, S., Helm, V., Skvarca, P. and Braun, M.: Changes in ice dynamics, elevation and mass discharge of Dinsmoor–Bombardier–Edgeworth glacier system, Antarctic Peninsula, Earth Planet. Sci. Lett., 427, 125–135, doi:10.1016/j.epsl.2015.06.047, 2015.

Shuman, C. A., Berthier, E. and Scambos, T. A.: 2001–2009 elevation and mass losses in the Larsen A and B embayments, Antarctic Peninsula, J. Glaciol., 57(204), 737–754, doi:10.3189/002214311797409811, 2011.

30   Stammerjohn, S. E., Martinson, D. G., Smith, R. C., Yuan, X. and Rind, D.: Trends in Antarctic annual sea ice retreat and advance and their relation to El Niño–Southern Oscillation and Southern Annular Mode variability, J. Geophys. Res. Oceans 1978–2012, 113(C3), 2008.

Steig, E. J., Schneider, D. P., Rutherford, S. D., Mann, M. E., Comiso, J. C. and Shindell, D. T.: Warming of the Antarctic ice-sheet surface since the 1957 International Geophysical Year, Nature, 457(7228), 459–462, 2009.

35   Strozzi, T., Luckman, A., Murray, T., Wegmuller, U. and Werner, C. .: Glacier motion estimation using SAR offset-tracking procedures, Geosci. Remote Sens. IEEE Trans. On, 40(11), 2384–2391, 2002.

Van der Veen, C. J.: Fundamentals of glacier dynamics, CRC Press, Rotterdam, The Netherlands., 2013.

Vaughan, D. G.: Relating the occurrence of crevasses to surface strain rates, J. Glaciol., 39, 255–266, 1993.

Vaughan, D. G. and Doake, C. S. M.: Recent atmospheric warming and retreat of ice shelves on the Antarctic Peninsula, 1996.

Vaughan, D. G., Mantripp, D. R., Sievers, J. and Doake, C. S. M.: A synthesis of remote sensing data on Wilkins Ice Shelf, Antarctica, Ann. Glaciol., 17, 211–218, 1993.

Vaughan, D. G., Marshall, G. J., Connolley, W. M., Parkinson, C., Mulvaney, R., Hodgson, D. A., King, J. C., Pudsey, C. J. and Turner, J.: Recent rapid regional climate warming on the Antarctic Peninsula, Clim. Change, 60(3), 243–274, 2003.

5   Wouters, B., Martin-Español, A., Helm, V., Flament, T., van Wessem, J. M., Ligtenberg, S. R. M., van den Broeke, M. R. and Bamber, J. L.: Dynamic thinning of glaciers on the Southern Antarctic Peninsula, Science, 348(6237), 899–903, doi:10.1126/science.aaa5727, 2015.

Zwally, H. J., Giovinetto, M. B., Jun, L., Cornejo, H. G., Beckley, M. A., Brenner, A. C., Saba, J. L. and Yi, D.: Mass changes of the Greenland and Antarctic ice sheets and shelves and contributions to sea-level rise: 1992–2002, J. Glaciol., 51(175), 509–527,

10   doi:10.3189/172756505781829007, 2005

Table 1: Parameter settings used for SAR intensity offset tracking.

Sensor	Sensor wavelength	Tracking window size (range * azimuth)	Step (range/azimuth)
ALOS PALSAR	23.5 cm L-band	128*384	12/36
ERS-1/2 SAR	5.6 cm C-band	256*1280	15/75
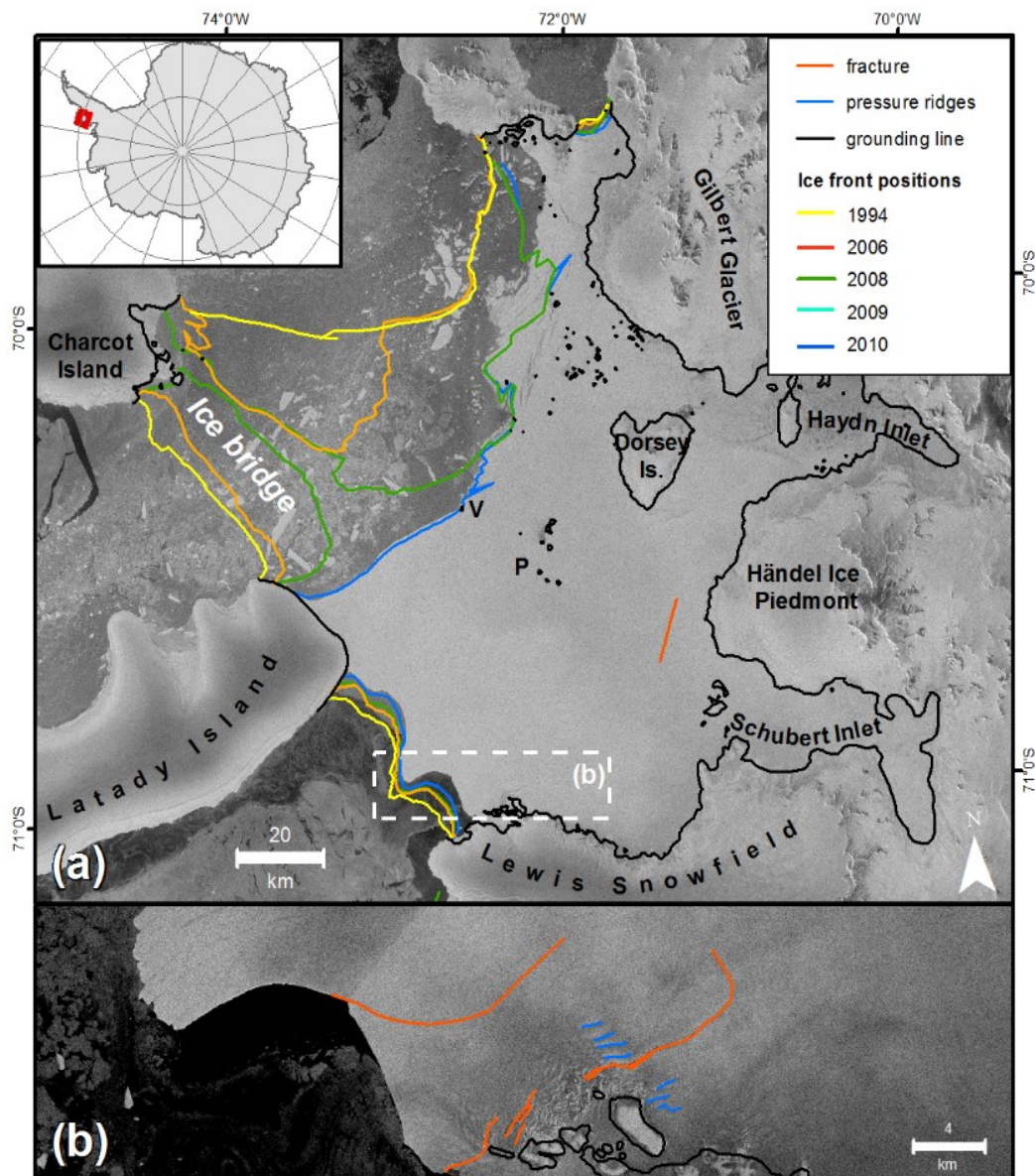
Figure 1: (a) Overview map of Wilkins Ice Shelf. The ice-front positions of the years 1994 and 2008 as well as the situation in 2015 are shown. The remnant ice connection (ice bridge) between Charcot and Latady Island in its shape from April 2008 is indicated. The location of the grounding line was derived from ERS-1/-2 differential interferometry (supplement material S3). (b) Fracture formation at the south-western ice front as detected between 2011 and 2015 from Envisat ASAR, Sentinel 1a and TanDEM-X imagery. P = Petrie Ice Rises, V = Vere Ice Rise. Background: Sentinel 1a 21-05-2015 © ESA.
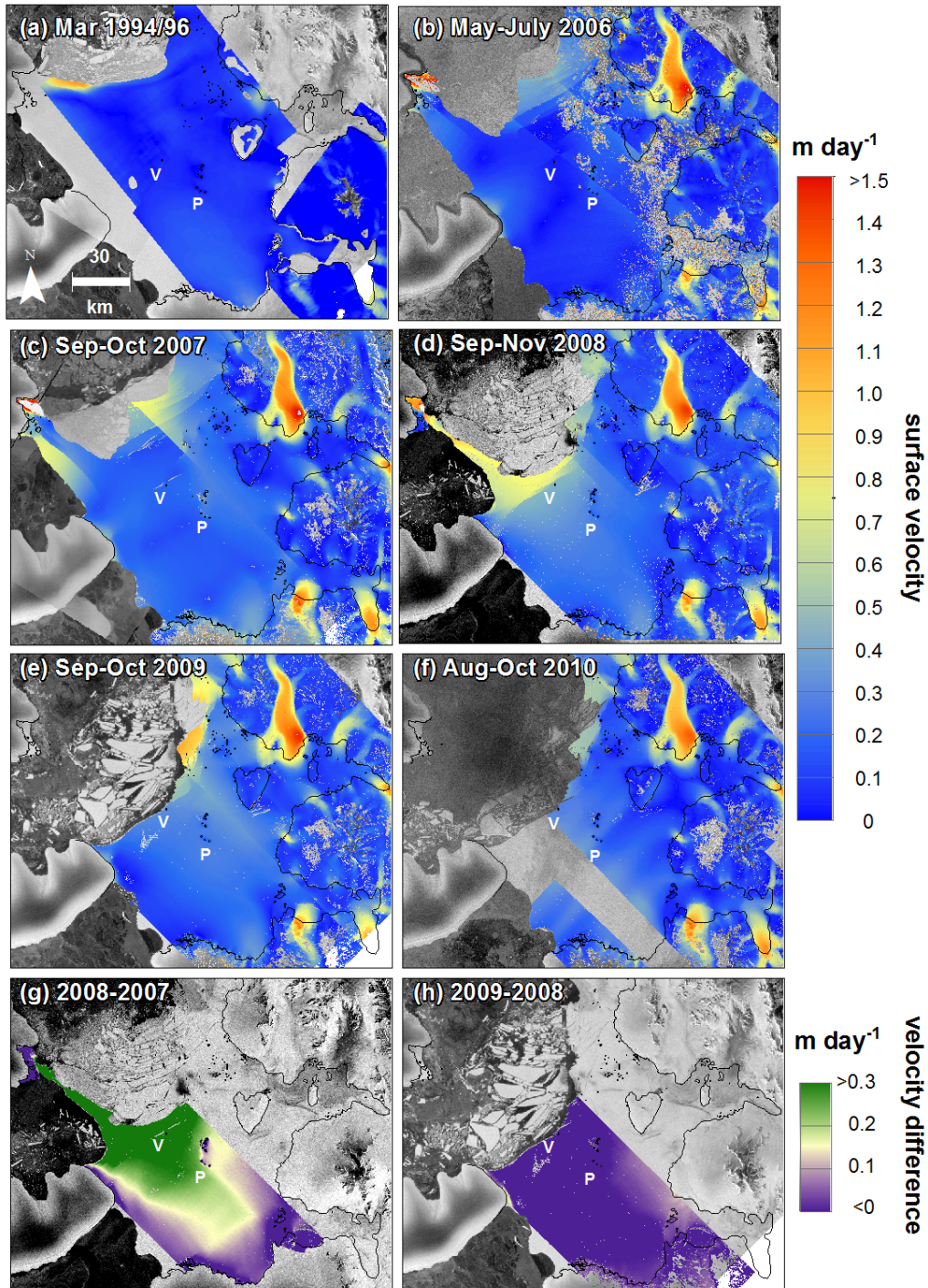
Figure 2: Surface velocities of WIS in 1994/96 and between 2006 and 2010 derived from ERS-1/2 (Braun et al., 2009) and ALOS PALSAR intensity offset tracking. The position of the grounding line in 1995/96 is marked as black line. Panels g) and h) show differences in surface flow between 2008 and 2007, and 2009 and 2008, respectively, for the western part of the ice shelf. P = Petrie Ice Rises, V = Vere Ice Rise. Background imagery: (a) MOA 2003/2004 © NSIDC, ERS-1/2 SAR 19-08-1993; (b) Envisat ASAR 25-03-2006; (c) Envisat ASAR 05-08-2007 and 09-09-2007; (d) Envisat ASAR 25-08-2008; (e) Envisat ASAR 22-07-2009; (f) Envisat ASAR 09-12-2010; (g) Envisat ASAR 25-08-2008; (h) Envisat ASAR 22-07-2009, © ESA.
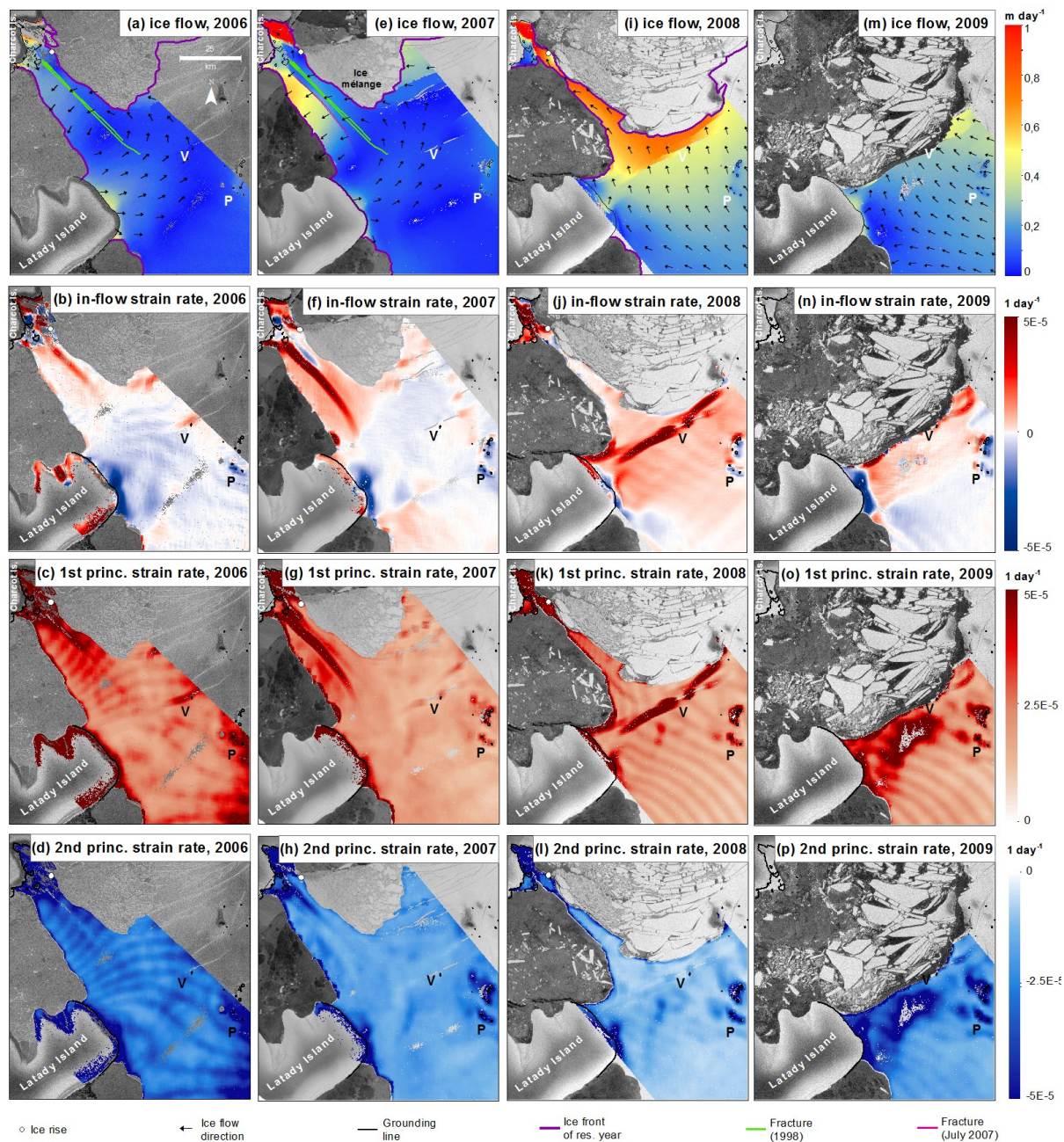
Figure 3: Surface velocities (first row), strain rates in flow direction (second row), first and second principal strain rates for the years 2006-2009 (bottom rows). For depiction, the strain-rate components were filtered using a moving average with a rectangular kernel of 1000m x 1000m. Arrows show the ice-flow direction above a threshold of 0.05 m day-1. For each date the respective ice-front positions are shown. A double fracture system formed in 1998 is shown as green lines in (a) and (e). A newly developed double fracture formed in July 2007 is marked as purple line in (e). P = Petrie Ice Rises, V = Vere Ice Rise. Background imagery: (a)-(d) Envisat ASAR 25-03-2006; (e)-(h) Envisat ASAR 09-09-2007; (i)-(l) Envisat ASAR 02-08-2008/06-08-2008; (m)-(p) Envisat ASAR 22-07-2009; © ESA.
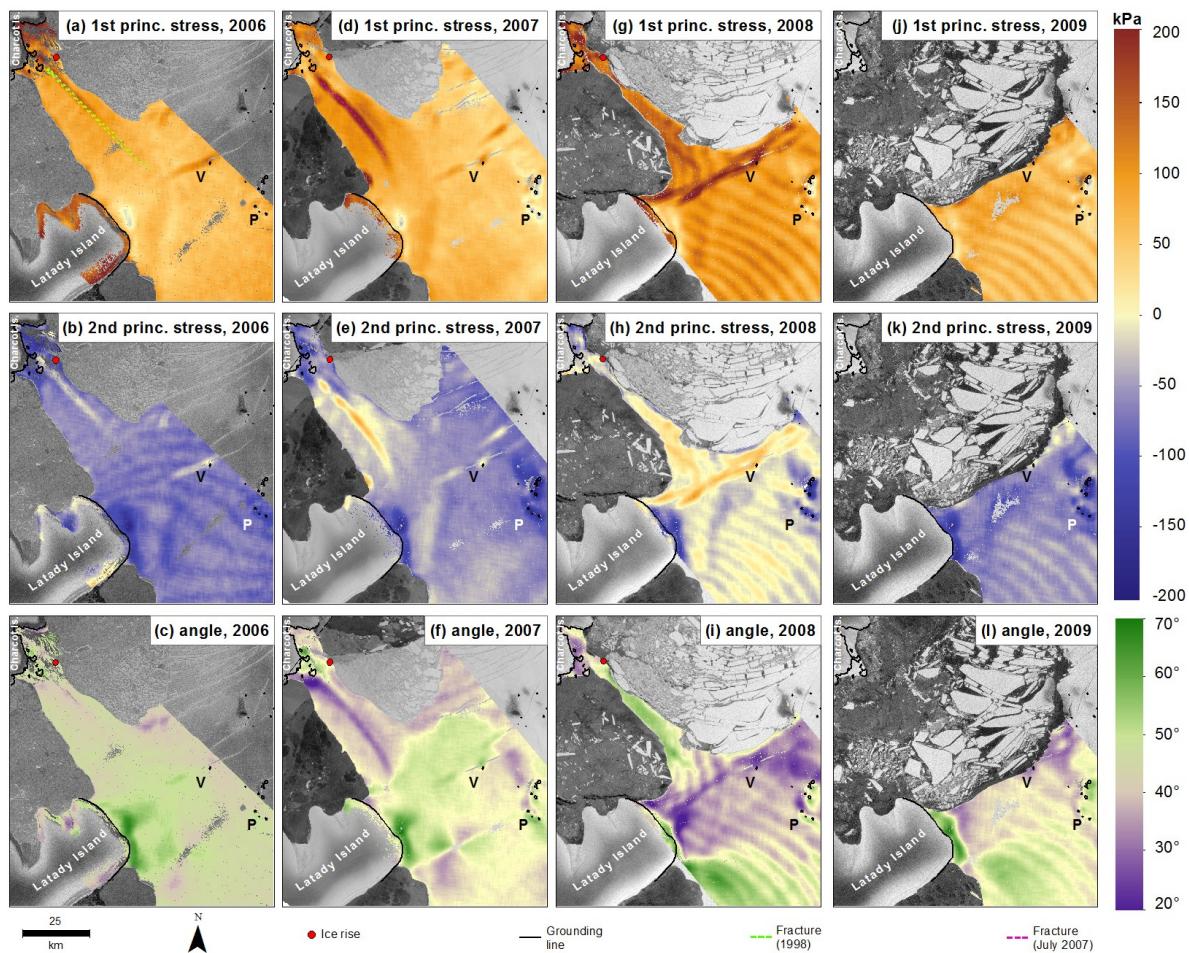
Figure 4: First and second principal stress fields as well as stress-flow angles on WIS for the years 2006-2009. P = Petrie Ice Rises, V = Vere Ice Rise. Background imagery: (a)-(c) Envisat ASAR 25-03-2006; (d)-(f) Envisat ASAR 09-09-2007; (g)-(i) Envisat ASAR 02-08-2008/06-08-2008; (j)-(l) Envisat ASAR 22-07-2009; © ESA.